

Hydro-dynamically modified seeding for micro-PIV

S. BŁOŃSKI¹⁾, P. DOMAGALSKI^{2,3)}, M. DZIUBIŃSKI²⁾,
T. A. KOWALEWSKI¹⁾

¹⁾*Department of Mechanics and Physics of Fluids
Institute of Fundamental Technological Research
Polish Academy of Science
Pawińskiego 5B
02-106 Warszawa, Poland*

²⁾*Faculty of Process and Environmental Engineering
Technical University of Łódź
Wólczajska 213
90-924 Łódź, Poland*

³⁾*Department of Process and Energy
and Department of Biotechnology,
Delft University of Technology
Delft, the Netherlands*

THIS PAPER PRESENTS NUMERICAL and experimental analysis of the hydrodynamic flow focusing in a rectangular microchannel. Aim of the study is to improve performance of the Particle Image Velocimetry (PIV) technique applied to micro-scale flow analysis. The symmetric flow focusing system of two channels crossed at right angle is investigated. The numerical model is used to analyse the effect of Reynolds number on the flow focusing mechanism. In the experiment, the flow focusing is applied to concentrate seeding tracers into a thin sheet at the channel axis. Such a modification removes the out of focus images of the seeding particles, effectively improving PIV evaluation of vector fields in microchannel. Based on the experimental and numerical results we have found that expected improvement is possible for the flow at Reynolds number less than 10 only.*)

Key words: selective seeding, flow focusing.

Copyright © 2011 by IPPT PAN

Notations

c mass concentration,
 d_H channel hydraulic diameter,
 d_p particle diameter,
 D diffusion coefficient,

*)The paper was presented at 19th Polish National Fluid Dynamics Conference (KKMP), Poznań, 5–9.09.2010.

e	spacing between sensor pixels,
κ	Boltzmann constant,
M	magnification,
n	refractive index, image pair number,
$NA = n \sin \theta$	numerical aperture,
Q	outlet stream flowrate,
Q_{F1}, Q_{F2}	focusing streams flow rates,
Q_S	focused stream flow rate,
R	pathline curvature radius,
$Re = Vd_H\rho/\mu$	Reynolds number,
S/N	signal to noise ratio, ratio of tracer peak intensity to mean background intensity,
t	time,
T	temperature,
V	velocity,
x	mean particle displacement,
δ_{corr}	depth of correlation,
δ_f	depth of focus,
θ	half-angle of objective-specimen light cone,
λ_0	light wavelength,
μ	dynamic viscosity of the fluid,
ρ	fluid density,
PIV	Particle Image Velocimetry,
SeS-PIV	Selective Seeding Particle Image Velocimetry,
Focusing ratio	– ratio of flow rate of the focused flow to the focusing streams $\left(\frac{Q_S}{Q_{F1} + Q_{F2}} \right)$.

1. Introduction

THE ADVANCES OF MICROFLUIDIC TECHNOLOGY have led to development of miniaturized devices for manipulating and sorting bio-samples, mixing and delivering chemical reagents, or encapsulating immiscible liquids. In most cases these devices use either simple T-shaped channels with two inlets side-by-side and one outlet, or two crossed channels with three inlets and one outlet. Mixing properties of such devices are often crucial for the effective functioning of microfluidic devices. Due to the characteristic dimensions of the devices, the flow Reynolds number is small and only molecular diffusion is responsible for the inter-diffusion of reagents [1, 2].

There is a class of microfluidic systems where flow mixing should be minimized. An example is the so-called flow focusing process, where the sample flow (supplied from the inlet channel) is constrained laterally within the centre of the microchannel by two neighbouring sheath flows from the side channels (see Fig. 1). In symmetric hydrodynamic focusing, the sample flow is constrained by two sheath flows to a relatively thin sheet at the channel symmetry (Fig. 2). By manipulating flow rates of the focusing flows, location of the focused sheet can be moved out of the symmetry plane. Achieving a precise control of the focused stream width is crucial in various applications of the flow focusing systems.

Due to the fabrication constraints, the flow focusing devices usually use straight channels of rectangular cross-section, of typically 50 to 100 μm and 5–10 mm length, interconnected at right angles. Flow in such microchannels is characterized by parallel streamlines and mixing of liquids/particles is mostly controlled by diffusion. However, even for very low Reynolds number regime, the abrupt change of the flow direction when fluid passes T junction, appears to produce secondary flow forcing fluid to move towards the side walls. It strongly affects both mixing as well as flow focusing efficiency. The effect is caused by two well-known mechanisms, so-called Moffat-eddies, created by the flow passing sharp corners, and Dean flow – secondary circulation generated due to the flow curvature. Both mechanisms, present even for very low Reynolds number flow, evidently change flow pattern and species distribution observed in the outlet channel. Experimentally it is observed as increase of the mixing zone or broadening of the flow-focused sheet, especially in the regions close to the side walls. The effect is important for the effectiveness of microfluidic devices and has to be considered by selecting proper flow regimes for working devices.

Here, we aim to apply flow focusing mechanism to improve quality of flow velocity measurements performed in microchannels. Such measurements are performed using micro Particle Image Velocimetry (micro-PIV), a non-intrusive technique for measuring flow fields with micron-scale resolution. Fundamentals of the micro-PIV method are based on microscopic images of the fluorescent tracers conveyed by an analysed flow and correlation analysis, applied to the subsequent pairs of images. Due to the small dimensions, the typical for macro-scale PIV light sheet technique cannot be applied for flow illumination and the whole investigated volume is flooded by light. Selection of analysed flow cross-section is based on the focal depth of optical system, as only tracers within the depth of focus are clearly visible. However, tracers out of focus participate in the image brightness as a background noise and evidently depreciate the evaluation accuracy. To overcome this drawback, low concentration of tracers is usually used and the performed correlation procedure averages the results over a large number of pairs of images. However, long averaging time limits the temporal resolution of the evaluated velocity field and creates problems with optimal tracers concentration if channel size suddenly varies.

Recently, the flow focusing method was proposed to introduce the tracers as a thin layer instead of whole volume seeding (SeS-PIV: Selective Seeding PIV [3]). Such layer can be obtained in rectangular cross-section channel via hydrodynamic focusing. Limiting seeding to a thin layer improves spatial resolution of the velocity field evaluation and permits to apply higher tracers concentration, hence allowing for acquisition of shorter sequences of images. As the position of focused stream can be controlled by manipulating flow rate of the

focusing streams, the SeS-PIV method opens a new possibility of 3D microflow reconstruction from several 2D flow fields taken at different channel depths.

In the following we investigate performance of this technique evaluating micro-flow over small protrusion introduced at one of the channel walls. Performance of such a protrusion as an element of flow mixing systems is often assumed to increase heat transfer in microscale [4]. Hence, flow velocity in vicinity of the protrusion is evaluated using micro-PIV data obtained by standard volume flow seeding and compared with the selective flow focusing seeding. Measurements are compared with each other and with a theoretical velocity field obtained from the numerical simulation. It is found that the advantages of selective seeding (SeS-PIV), well visible for low Reynolds number flow ($Re < 10$), are strongly depreciated increasing flow rate due to subsequent broadening and deformation of the focused sheet of tracers.

2. Experimental setup

A polymeric device was fabricated to visualize performance of the flow focusing device (Fig. 1). The device was made of 5 mm thick polymethylmethacrylate (PMMA) and consists of two crossed rectangular channels of $300 \mu\text{m} \times 420 \mu\text{m}$ cross-section made by micro-milling. The two side-by-side inlets are used to pump the focusing fluid Q_F . The focused fluid with seeding Q_S was pumped through the central inlet. A small ($90 \mu\text{m} \times 90 \mu\text{m}$) protrusion (rib) was made 5 mm downstream from the intersection at the bottom wall of the outlet channel, to monitor stability of the focused sheet and to evaluate performance of the PIV measuring technique. The rib height was chosen to generate apparent modification of the channel flow pattern, allowing to compare performance of the standard micro-PIV and modified SeS-PIV technique for complex flow structure built in its vicinity.

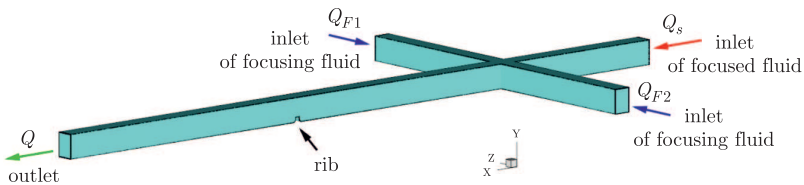


FIG. 1. Schematic of the investigated flow focusing microfluidic device. Flow images are taken around small rib made at the bottom wall of the outlet channel.

The flow around the protrusion was analyzed using *in-house* built micro-PIV [5] system based on Nikon Eclipse E-50i epi-fluorescent microscope, long working distance objective 10x/0.3 WD 17.5 (Nikon LU PLAN FLUOR) and SensiCam Double Shutter 12-bit CCD camera with resolution 1280×1024 pixels

(PCO IMAGING). The illumination was provided by SoloPIV Nd:YAG double-pulsed laser (532 nm) from New Wave Research Inc. The flow was forced by three syringe pumps (New Era Pump Systems Inc.). The total flow rate was maintained between $Q = 1.45 \cdot 10^{-10} \text{ m}^3/\text{s}$ and $Q = 1.87 \cdot 10^{-8} \text{ m}^3/\text{s}$, what corresponds to Reynolds number $Re_{\min} = 0.4$ and $Re_{\max} = 50$. The focusing ratio, defined as the ratio of flow rate of the focused stream to the focusing streams ($Q_S/(Q_{F1} + Q_{F2})$) is an important parameter and its optimal value was found to be 1 : 20. For low Reynolds number flow this ratio gave us stable, about $15 \text{ }\mu\text{m}$ thin sheet of focused flow.

Deionised water and fluorescent tracers (Fluorescent Polymer Microspheres $2 \text{ }\mu\text{m}$, Duke Sci.) were used as media. Particle tracing was applied to visualize flow structure at the crossing area of the focusing device (Fig. 2). For PIV measurements, fluorescent tracers were introduced to the focused stream and their images were acquired by the PIV camera for subsequent flow velocity evaluation. The tracers volume concentration was kept very low, hence it is assumed that their effect on the flow is negligibly small. For the micro-PIV measurements, the tracers concentration was set to be $c_{\text{PIV}} = 0.00909\%$. In case of selective seeding (SeS-PIV) it was possible to increase seeding concentration ten times ($c_{\text{SeS-PIV}} = 0.0909\%$) without visible depreciation of the flow images. Higher seeding concentration permits to collect sufficient number of PIV images in a shorter time and this is one of important goals of the proposed method.

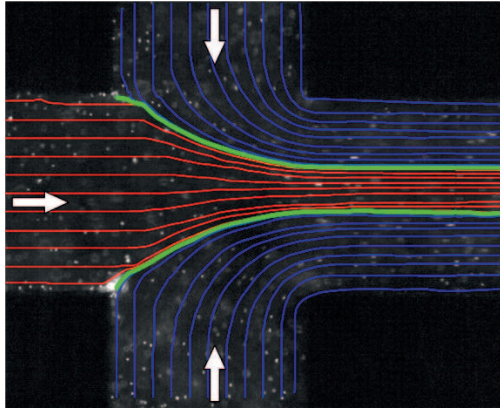


Fig. 2. Visualization of the flow focusing mechanism: particle tracks evaluated for fluorescent tracers passing the crossing region of the flow-focusing channels; to visualize the flow structure, tracers were introduced to focusing (blue paths) and to focused (red paths) flow. The green contour indicates thickness of the focused sheet.

Performance of the PIV evaluation was investigated using flow images around the rib region, taken perpendicularly to the flow direction (Fig. 1). The acquired flow images cover an area of $0.4 \text{ mm} \times 0.8 \text{ mm}$ and are obtained by

the microscope focused at the channel centre. Each PIV measurement consisted of a sequence of 100–200 pairs of images taken at intervals of 0.25 s. Each pair of images was obtained illuminating the channel by double pulsed laser at time intervals matched to the flow velocity and magnification factor of the system. This time varied from 50 μs to 5 ms for the range of applied flow rates.

Our preliminary experimental investigations indicated that focused flow sheet is not necessarily uniform and its thickening close to the walls may reach undesirable value [6, 7]. Three-dimensional study of this effect performed by using confocal microscopy [8] confirmed that focused sheet is not flat and with increasing flow rate it exhibits nearly tripled thickness at both side walls (Fig. 3).

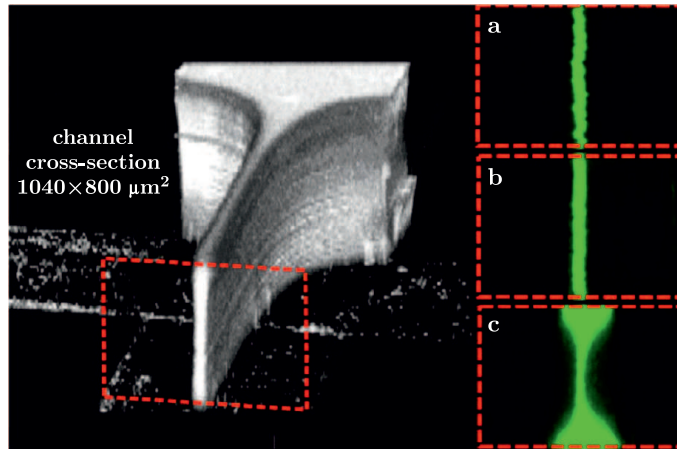


Fig. 3. Flow focusing observed under confocal microscope; a, b, c – thickening of the focused plane closed to the side walls, observed when increasing the flow rate (Reynolds number equal to: a) 3.23, b) 6.46, c) 12.92) [8].

Undesired thickening of the focused sheet including tracers may effectively decrease accuracy of the PIV evaluation close to the wall. In the following numerical study we aim to analyse main features of the flow focusing device and to elucidate the role of the flow parameters responsible for its proper performance.

3. Flow focusing numerical analysis

The steady, laminar and isothermal flow of viscous incompressible liquid is analyzed using finite volume code Fluent 12 (Ansys Inc) [9]. A three-dimensional (3-D) mesh representing the flow focusing device used in the experiment was built using Gambit 2.6 (Fluent Inc). The geometry and dimensions of the CFD model were identical to the experimental device. The boundary conditions were set as a mass flow at the inlets and as pressure at the outlet.

Different meshes were tested until mesh refining had little effect on the computations results. Finally, several simulations were performed with the structural hexahedron mesh of over 11 million cells by varying flow rate to cover Reynolds number from 0.1 to 100 (Fig. 4).

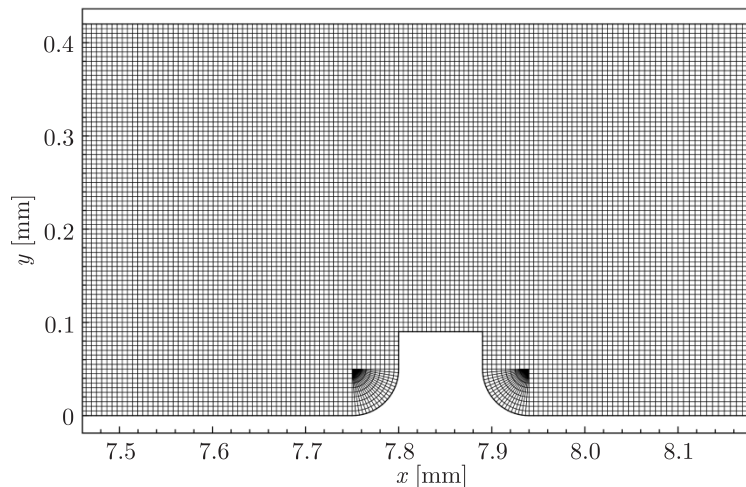


FIG. 4. Computational grid in the vicinity of the rib, used in numerical simulations.

In the experiment, the focusing performance of the system was analyzed by introducing small ($2\ \mu\text{m}$) florescent particles to the focused liquid and observing their concentration in the outlet channel. In the numerical model, to determine flow structure and shape of the focused layer containing fluorescent tracer particles, we used non-reacting species transport model with two liquids having the same physical and chemical properties (pure water without particles). The mass diffusivity coefficient of the focused fluid was set as $D = 2.22 \cdot 10^{-13}\ \text{m}^2/\text{s}$ to mimic the diffusivity of tracer particles. This was calculated as the diffusivity of the large, spherical particles in low molecular weight solvent [10]. We neglect any inter-particle and particle fluid hydrodynamic interactions, assuming that tracers are neutrally buoyant and the particle Reynolds number [11] is less than 10^{-3} .

Having fixed geometry of the system used in the experiment we have investigated the role of two parameters responsible for the flow focusing, namely the ratio of the focused to focusing flow rates and the flow Reynolds number at the outlet channel. Figure 5 demonstrates numerical simulation of the focusing effect obtained for the Reynolds number equal to 0.4 and focusing ratio equal 1 : 20. A thin sheet of the focused fluid is visible in the centre of the outlet channel. It is evident that thickness of the focused plane remains practically constant over a long distance from the crossing region of the inlet channels. Obviously, diffu-

sion of the focused seeding is negligible small. Even after passing the obstacle made at the bottom wall (see Fig. 5), undisturbed sheet of the focused flow is fully recovered. Small diffusivity of particles confirms rough estimation of the diffusion distance based on the diffusion constant and flow velocity, indicating that on their way down the flow, the particles may diffuse the distance of less than $0.1 \mu\text{m}$. Such behaviour permits to use the system for selective seeding flow velocity evaluation (SeS-PIV) as it is clearly visible that despite the long distance travelled through the outlet channel and presence of the obstacle located on the way, thickness of the focused sheet remains all the way constant and equal to about $17 \mu\text{m}$.

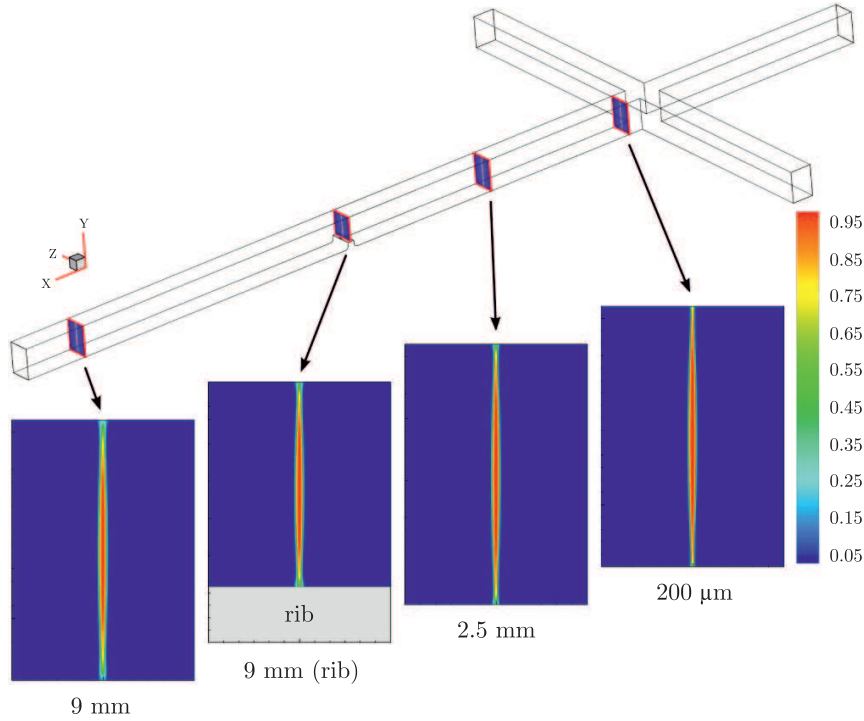


FIG. 5. Flow focusing obtained from numerical model for Reynolds number 0.4. Focusing ratio 1 : 20.

Numerical simulation performed for four different focusing ratios indicates that thickness of the focused plane decreases with increase of the focusing ratio (Fig. 6). However, very strong effect on the focused sheet structure is observed by varying total flow rate, i.e. the flow Reynolds number (Figs. 6 and 7). Increasing the Reynolds number above 10 practically destroys flow focusing mechanism and for Reynolds number above 50, the focused fluid is fully layered on the top and bottom walls, being absent from the channel center.

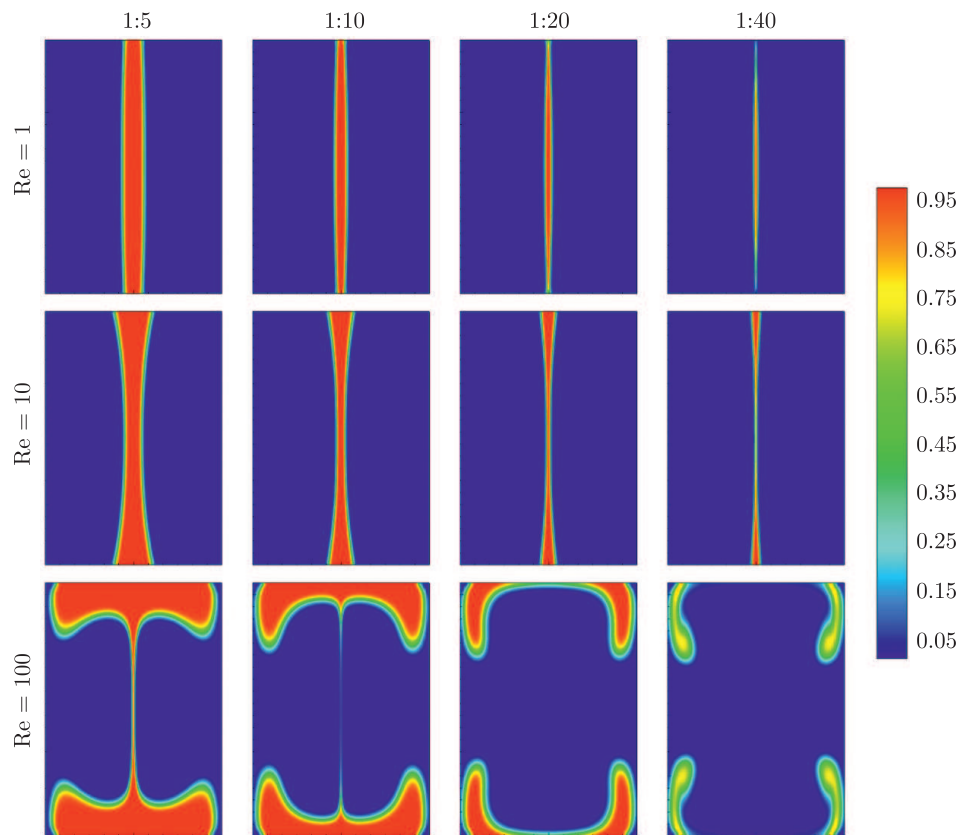


FIG. 6. Distribution of the focused fluid for three different Reynolds numbers (rows) and four different focusing ratios (columns).

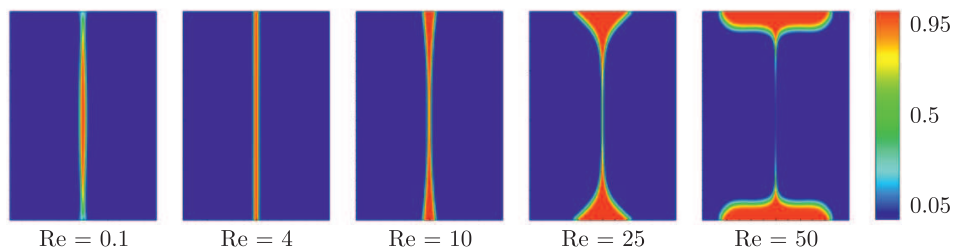


FIG. 7. Effect of Reynolds number: distribution of the focused fluid for flow Reynolds numbers $Re = 0.1$, $Re = 4$, $Re = 10$, $Re = 25$ and $Re = 50$. Focusing ratio is $1:20$.

Numerical simulations clearly indicate three regimes of the flow focusing mechanism:

- Regular, well defined, nearly flat focused plane can be obtained for Reynolds number 4. Smaller Reynolds number creates a slightly convex shape.

- Double concave shape is present for Reynolds number above 10.
- Complete layering of the focused flow on the side walls takes place for Reynolds number approaching 100.

Numerical analysis indicates that the source of the observed disturbances is located in a small region where three streams merge together to the outlet channel. It is worthy to repeat that molecular diffusion is completely negligible in the analysed case. Hence, the geometry of the focused plane, once created by three merging streams, remains unchanged along the outlet channel. For low

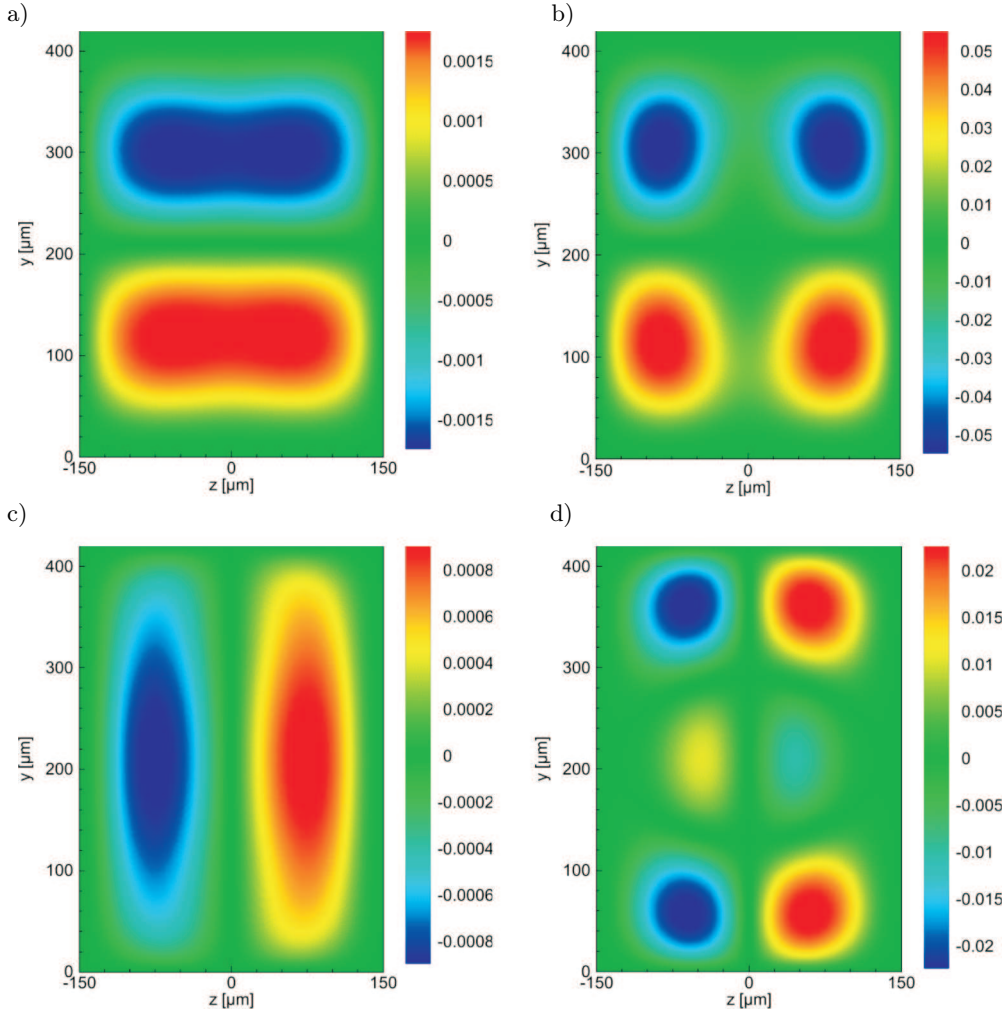


Fig. 8. Normalized V_y velocity component (upper row) and V_z velocity component (lower row), obtained for the outlet channel cross-section 200 μm behind the crossing area; for two Reynolds numbers: $Re = 0.4$ (left-hand column), $Re = 25$ (right-hand column). Note the change of scale when comparing left- and right-hand columns.

Reynolds number flow there are only two possible mechanisms responsible for the observed deformation of the focusing plane, so-called Moffat-eddies [12, 13], created by the flow passing sharp corners, and Dean flow – secondary circulation generated due to the flow curvature [14–16]. Both mechanisms are responsible for deformation of the velocity pattern, visible in Fig. 8. It can be seen that both transversal velocity components responsible for the secondary flow increase over 30 times their relative value for higher Reynolds number (Fig. 8, right column). We may note concentration of the secondary flow into well-visible spots in four corners of the channel. The cross-flow found in the corners is responsible for the lateral transport of liquid and effectively for broadening of the focused sheet at the top and bottom walls.

Figure 9 collects the results of numerical investigations by displaying normalized cross-flow velocity as a function of distance and Reynolds number. One may find that strong lateral flow components are present only in the vicinity of the crossing area. It is the place where the main redistribution of particle concentration takes place. At larger distances (over 1 mm, i.e. 3 channel diameters), the parabolic flow profile is fully established preserving disturbed concentration distribution. The effect of Reynolds number is clearly visible, the relative value of the lateral flow velocity increases with Reynolds number and its presence decreases with the distance.

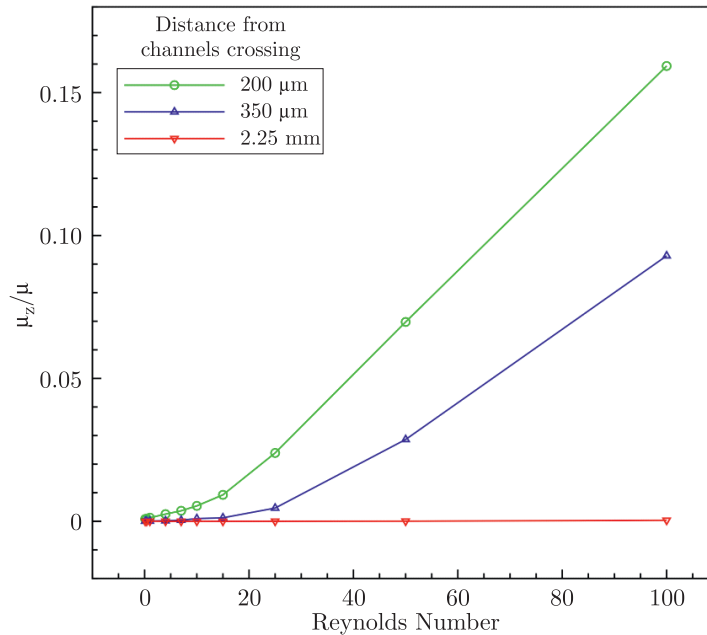


Fig. 9. Normalized (by mean velocity) maximum value of the z -component of the velocity vs. Reynolds number, monitored at three different distances from the channels crossing.

4. Selective Seeding PIV technique: advantages and limitations

As we mentioned, measuring volume of the micro-PIV technique depends on depth of focus of the microscope and all visible particles are participating in the correlation of images used for the velocity field evaluation. In addition, particles above and beneath the focal plane are contributing to the image by blurring background light. The value of depth of focus δ_f is predefined by an optical system of the microscope and cannot be easily modified. The whole depth section of the flow contributing to the measured velocity field is called the depth of correlation δ_{corr} . Physically it is the depth of focus of the microscope, extended by effects of diffraction and tracer particles geometry. Analytically derived, and confirmed experimentally, the formula for the depth of correlation was defined by MEINHART [17] as:

$$\delta_{\text{corr}} = \frac{2.16d_p}{\tan \theta} + \frac{3n\lambda_0}{NA^2} + \delta_f,$$

$$\delta_f = \frac{n\lambda_0}{NA^2} + \frac{ne}{NA M},$$

where, d_p – particle diameter, n – refractive index, NA – numerical aperture, λ_0 – light wavelength, M – magnification, e – the smallest distance that can be resolved by a detector located in the image plane of the microscope (for the case of a CCD sensor, e is the spacing between pixels) and θ can be determined from $NA = n \sin \theta$.

For our experimental setup the calculated depth of correlation was 36 μm , i.e. 12% of the channel depth. To take the advantage of tracers confined in thin layer focused in the channel centre, the thickness of the focused stream has to be kept below the depth of correlation threshold. In our case, the control over the focused stream thickness was gained by setting the focusing ratio of 1 : 20. Simple estimation based on the flow rate ratio and change of channels cross-sections gives for the investigated configuration the focused stream thickness equal to 15 μm . However, as it is shown in the previous chapter, the focused stream preserves its sheet-like, two-dimensional shape only for Reynolds number less than 10. For higher Reynolds number, the focused sheet becomes wider near the top and bottom walls and thinner at the middle and this deformation grows with increasing Reynolds number (cf. Fig. 7). Hence, proper selection of the flow parameters is crucial for obtaining improved seeding for SeS-PIV.

4.1. Image analysis

At the first step, the effect of the flow focusing applied for SeS-PIV can be demonstrated by comparing quality of the raw images obtained by both methods (see Fig. 10). Indeed, at the first glance one may find better contrasts of the

image with focused seeding (Fig. 10b). Practically all particles are in focus for selective seeding, while the volume seeding (Fig. 10a) generates strong background originating from out-of-focus particles. What is more, the tracers are flowing in a thin layer, thinner than depth of focus, so their images lack the diffraction rings as opposed to out-of-focus particles present in the micro-PIV picture. However, there is a visible additional blurred area near the obstacle in SeS-PIV picture, which appears due to the three-dimensional deformation of the focused stream when it passes the rib. The cross-flow behind the rib is responsible for tracers redistribution in depth and so they are no longer in depth of focus. This effect was observed only at the highest tested velocities ($Q > 1.87 \cdot 10^{-8} \text{ m}^3/\text{s}$ and $Re > 50$), what confirms numerically predicted limitations of the flow focusing method.

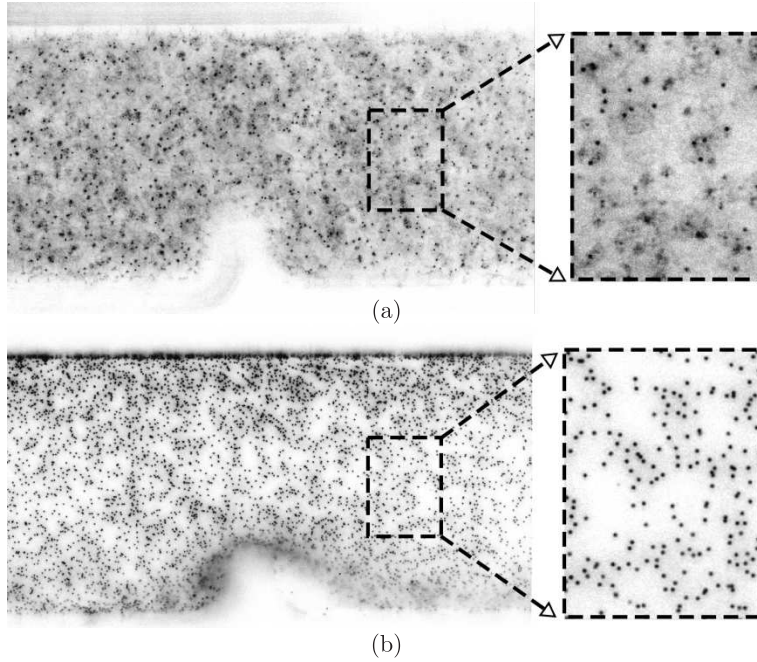


Fig. 10. Image of tracers passing the rib and magnified fragment; a) volume seeding for micro-PIV; b) selective seeding used for SeS-PIV technique; $Re = 50$, focusing ratio 1 : 20 for both cases.

The drastic reduction of the background noise in case of SeS-PIV images corresponds to higher signal to noise ratio (S/N) and improves the PIV evaluation. For current purpose the S/N ratio was defined as a ratio of tracer peak intensity to mean background intensity [17] and it was calculated for full, single captured image frame. Figure 11 shows the comparison of so evaluated S/N ratio plotted against the correlation depth, calculated for micro-PIV optical system (full blue circle) or taken as thickness of the focused seeded layer for SeS-PIV

experiment (full red square). In addition, it is compared with the available literature data [17] (open blue circles) obtained from typical micro-PIV experiments. The presented data were collected during experiment with total flow rate set as $Q = 1.87 \cdot 10^{-8} \text{ m}^3/\text{s}$ for microPIV and about $Q = 2.3 \cdot 10^{-9} \text{ m}^3/\text{s}$ for SeS-PIV. As visible on Fig. 11 the selective seeding results in over two-fold increase of the signal to noise ratio (S/N) and evidently, a thinner correlation depth formed by focused sheet of tracers than the parameters achieved by optical systems of micro-PIV configurations. Additionally, the correlation depth defined by the focused sheet can be controlled by flow parameters, even down to the width of nm order [18], independent on optical setup.

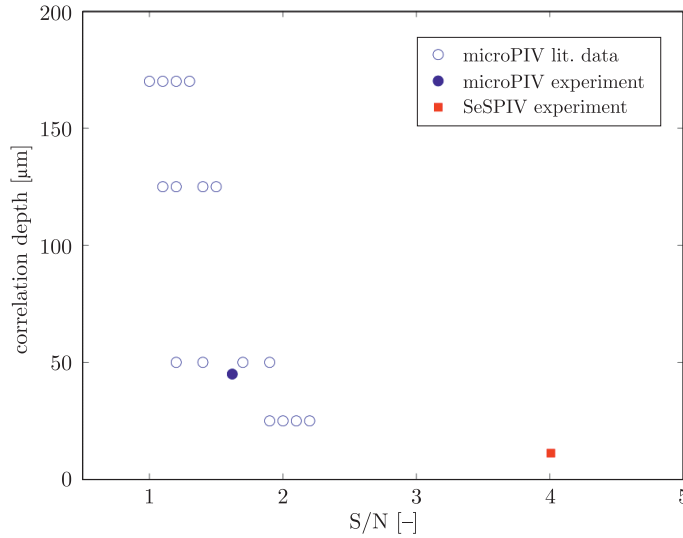


Fig. 11. Signal to noise ratio (S/N) as a function of test section depth (correlation depth) obtained for micro-PIV technique and for selective seeding PIV system. Present experiments are compared with available literature data [17] for micro-PIV systems.

4.2. Evaluation of PIV convergence

As it was mentioned above, the images obtained by a typical micro-PIV system are outshined by large amount of blurred out-of-focus tracers. As a result, very low concentration of seeding has to be used. To obtain sufficient amount of data for the PIV evaluation, long sequences of images are collected and averaged. Time necessary to obtain such a sequence seriously limits the temporal resolution of the system. In the following we demonstrate advantage of the selective seeding, where total time of image acquisition can be reduced by reducing the number of image pairs needed for obtaining well resolved flow field. To address this issue we analyse variation of an averaged flow field as a function of the number

of evaluated velocity fields taken to calculate the average. As a reference, the velocity field averaged over 200 image pairs is used.

It can be found in Fig. 12 that for lower Reynolds numbers, the SeS-PIV technique converges much faster than standard micro-PIV. The average of the longitudinal velocity component (a) appears to be correct for SeS-PIV evaluation of less than 10 pairs of images. The micro-PIV evaluation needs over 20 pairs of images to converge. The described tendency is less clear in case of the vertical velocity component (V_y , not shown). This cross-flow velocity component is by one order of magnitude smaller and lack of resolution is mainly due to the limits of the PIV evaluation method (tracer displacement in vertical direction are of the order of the camera pixel size).

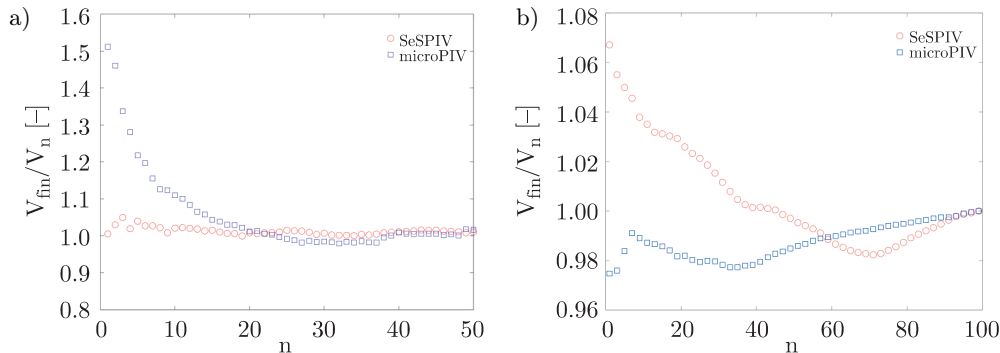


Fig. 12. Convergence of the averaged longitudinal V_x velocity component obtained by micro-PIV (blue squares) and SeS-PIV method (red circles), as a function of number of fields used for PIV correlation; two flow rates: a) $Q = 1.45 \cdot 10^{-10} \text{ m}^3/\text{s}$ ($\text{Re} = 0.4$), b) $Q = 0.935 \cdot 10^{-8} \text{ m}^3/\text{s}$ ($\text{Re} = 25$).

For higher flow Reynolds number, the PIV evaluation needs longer sequences of images to converge. The right-hand part of Fig. 12 represents evaluation done for Reynolds number 25. As we may find, both PIV techniques require more than 100 image pairs to converge the averaged evaluation. There is no visible difference between the micro-PIV and the SeS-PIV method. It is due to the aforementioned deformation of the focused stream appearing at higher Reynolds number (Fig. 7), thus thickness of the focused sheet carrying tracer is bigger than the depth of correlation. In such a case there is no difference between the both techniques except for the channel centre. It shows limits of the SeS-PIV technique.

4.3. Comparison with numerical results

The main purpose of any PIV evaluation is to obtain full, two-dimensional velocity field of an interrogated flow region. Such data are valuable for understanding flow structure and for validating numerical simulations. Hence, in the follow-

ing we compare flow fields obtained by both PIV techniques with their numerical counterparts obtained for the same configuration. The comparison is done for the two flow rates $Q = 1.45 \cdot 10^{-10} \text{ m}^3/\text{s}$ ($\text{Re} = 0.4$) and $Q = 0.935 \cdot 10^{-8} \text{ m}^3/\text{s}$ ($\text{Re} = 25$). The PIV analysis is performed in both cases using 5 image pairs to obtain averaged flow fields. Both PIV evaluation techniques offer reasonable results, qualitatively comparable with the numerical prediction. However, Fig. 13b clearly indicates that in case of the micro-PIV technique the vector field deviates from its numerical prediction (Fig. 13c) in the neighbourhood of the rib. Evidently, the flow pattern deformation present close to the rib is smoothed out by evaluation of micro-PIV images. Proposed selective seeding PIV method demonstrates its advantage.

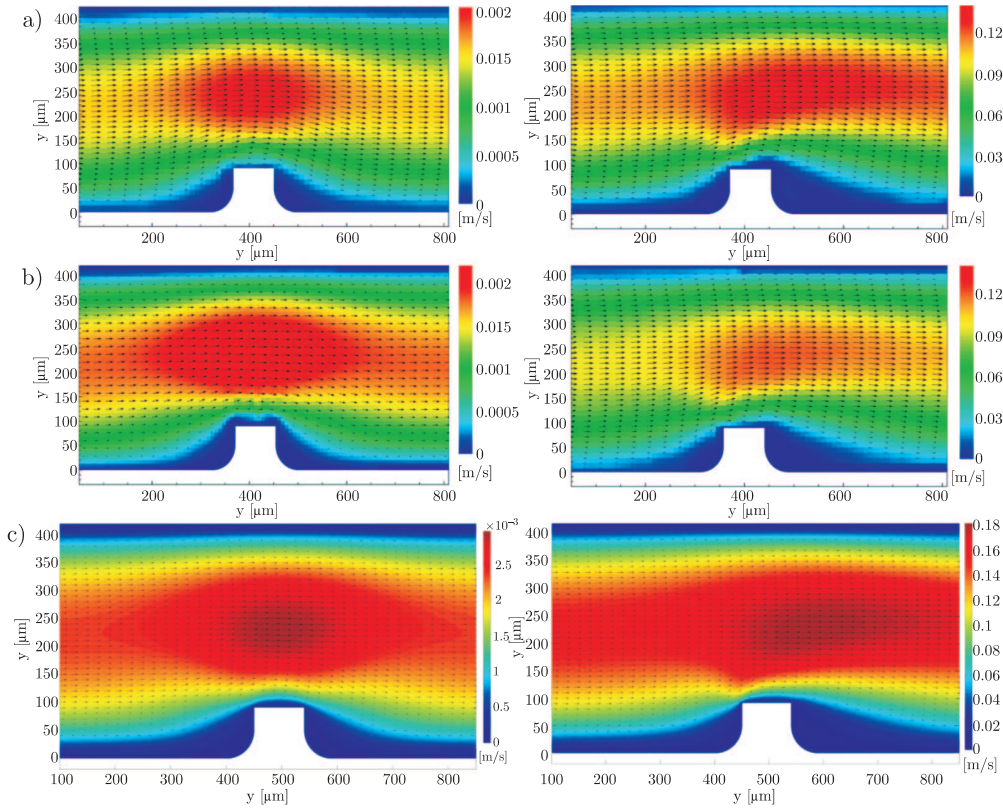


Fig. 13. The comparison of flow fields obtained by: a) SeS-PIV, b) micro-PIV, c) built from 5 image pairs and predicted by the numerical simulation. Left-hand column: flow rate $Q = 1.45 \cdot 10^{-10} \text{ m}^3/\text{s}$ ($\text{Re} = 0.4$); right-hand column: flow rate $Q = 0.935 \cdot 10^{-8} \text{ m}^3/\text{s}$ ($\text{Re} = 25$).

More quantitative analysis of the differences between both measurements and the numerical prediction is given in Fig. 14. At lower Reynolds number (Fig. 14a), a micro-PIV appears to overestimate value of the velocity evaluated

for the channel centre. It is possible that number of averaged images (5) is too small for the micro-PIV evaluation. It correlates with the previous observation (cf. Fig. 12) that micro-PIV technique notoriously overestimates flow velocity if there are not enough flow fields used for the averaged value. On the other hand, at higher flow rates (Fig. 14b) typical micro-PIV evaluation underestimates the value of measured flow velocity. It is due to relatively large correlation depth which is responsible for averaging information collected from different cross-sections of the flow. The selective seeding methodology avoids these errors, except for the regions in the vicinity of the rib (bottom part of the velocity profile).

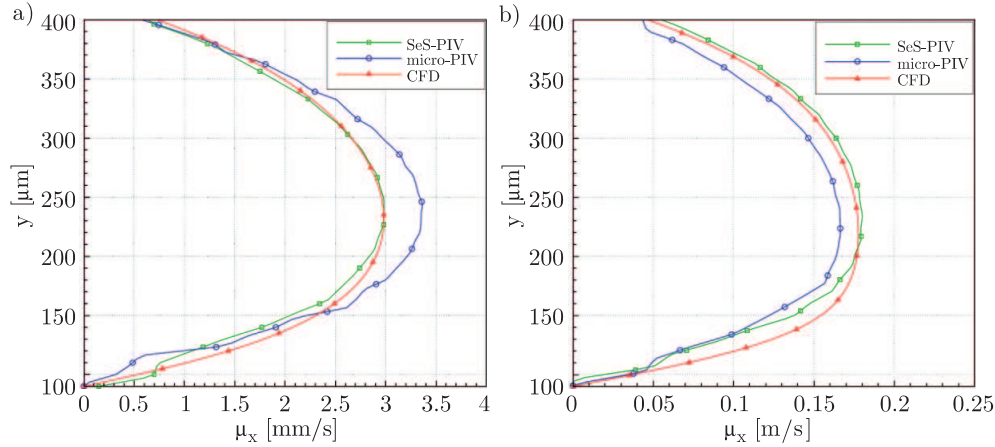


Fig. 14. Vertical profile of the x -component of velocity above the rib: comparison of the numerical (CFD) and experimental results (SeS-PIV and micro-PIV) for Reynolds number: a) $Re = 0.4$ and b) $Re = 25$.

4.4. General discussion of SeS-PIV applicability

The application range of SeS-PIV is directly connected with hydrodynamics of the focusing technique, as it relies on the shape and stability of focused flow sheet with tracers. Our numerical study given above clearly indicates limitation due to the inertia (Reynolds number). There are two mechanisms responsible for creation of double concave shape, namely the inertia driven Dean flow and the diffusion.

The Dean flow is a secondary flow pattern developing due to imbalanced centrifugal force when fluid element is moving along a curved path. In case of flow focusing, the side streams change the flow direction and all focussed flow pathlines bend at 90 degree angle. Thus in cross-section after the joint the secondary Dean flow pattern is developed in form of two pairs of counter rotating circulation zones.

The significance of this recirculation on focused stream deformation is a function of Reynolds number and geometry. The relation in form of the Dean number describing dimensionlessly this ratio is given as $\text{Re}\sqrt{d_H/2R}$, where d_H is the channel characteristic diameter and R is the pathline curvature radius.

The importance and influence of Dean flow is diminishing in lower Re range corresponding to the observed flat, focused stream across the channel for $\text{Re} < 10$. Entering the creeping flow regime ($\text{Re} < 1$) extinguishes the inertia-based Dean flow, however the rising viscosity domination gives the birth to another phenomenon, namely to formation of Moffat eddies [12, 13]. This means that in proximity of stagnation points (corners), where the liquid-wall contact surface is relatively big, the different circulation zones are formed. The change from Dean to Moffat eddies as the responsible focused stream deformation source corresponds to changes in its shape.

The second source of focused stream deformations, after the hydrodynamics, is molecular diffusion. It has negligible effect for relatively large seeding particles used in the experiment described above. However, in several microfluidic applications seeding particles as small as 20 nm (quantum dots) are applied. Hence, the diffusion effect should be discussed. Generally the particle mean displacement due to diffusion can be estimated as square root of the diffusion time and diffusivity $x = \sqrt{2Dt}$, with estimation for diffusion constant for spherical particles (neglecting solvent-tracer interaction) as $D = \kappa T / (3\pi\mu d_p)$, where κ is Boltzmann constant, T – temperature, μ – viscosity of the fluid and d_p – particle diameter. In our case, for 2 μm particles D is of order of magnitude 10^{-13} [m^2/s] and the length scale of the diffusion is negligibly small (around 1 μm). Obviously, for 100 times smaller tracers (e.g. 20 nm quantum dots) the effect of diffusion length becomes no longer negligible, diminishing the advantages of the flow-focusing technique. Additionally the diffusion-convection coupling of tracer particles in the near wall regions will render the net diffusion effect more intense in those areas, broadening the double concave shape of the focused sheet [19–21].

Summary and conclusions

We have confirmed the advantages of modified micro-PIV technique by introducing the thin, hydrodynamically focused layer of tracers. Such modification known as SeS-PIV technique improves the raw image quality by removing the background noise, increases the signal to noise ratio, and most important – permits higher seeding concentration. These features directly correspond to the improved resolution of obtained vector fields and to shorter time of analysis. It allows for taking instantaneous flow field with well resolved details. In addition, the noticeable decrease of out-of-focus background light allows to use

this technique at low light conditions. The aforementioned improvements of microflow analysis are possible if the flow Reynolds number remains low enough ($Re < 10$).

Acknowledgements

This work was supported by Ministry of Science and Higher Education of Poland as research project No. N N20829433 “Badanie ogniskowania hydrodynamicznego cieczy w węźle mikrokanalów” and N N501008733 “Intensyfikacja procesu mieszania w mikroprzepływach”.

References

1. J.M. OTTINO, S. WIGGINS, *Introduction: mixing in microfluidics*, Phil. Trans. R. Soc. Lond. A, **362**, 923–935, 2004.
2. N.T. NGUYEN, Z. WU, *Micro-mixers – a review*, Journal of Micromechanics and Micro-engineering, **15**, 1–16, 2005.
3. M.M. MIELNIK, L.R. SAETRAN, *Selective seeding for micro-PIV*, Experiments in Fluids, **41**, 155–159, 2006.
4. O. ALSHROOF, J. REIZES, V. TIMCHENKO, E. LEONARDI, *Flow structure and heat transfer enhancement in laminar flow with protrusion-dimple combinations in a shallow rectangular channel*, Proceedings of the ASME Summer Heat Transfer Conference 2009, HT2009 2, pp. 785–795, July 19–23, 2009, San Francisco, CA, U.S.A.
5. S. BŁOŃSKI, P.M. KORCZYK, T.A. KOWALEWSKI, *Analysis of turbulence in a micro-channel emulsifier*, International Journal of Thermal Science, **46**, 1126–1141, 2007.
6. P. DOMAGALSKI, M. DZIUBIŃSKI, S. BŁOŃSKI, T.A. KOWALEWSKI, *Zastosowanie ogniskowania hydrodynamicznego jako modyfikacji techniki micro-PIV*, I Krajowa Konferencja Nano- i Mikromechaniki, Krasiczyn, 8–12 lipca, Wyd. Polit. Rzeszowskiej, 2008.
7. S. BŁOŃSKI, P. DOMAGALSKI, T.A. KOWALEWSKI, *Flow focusing in microfluidic devices*, 19th Polish National Fluid Dynamics Conference (KKMP2010), 5–9.09.2010, Poznań, Poland.
8. P.M. DOMAGALSKI, M. DZIUBIŃSKI, P. BUDZYŃSKI, M.M. MIELNIK, L.R. SAETRAN, *Width variations of hydrodynamically focused streams in low to moderate Reynolds number*, Proceedings of European Conference of Chemical Engineering (ECCE-6), Copenhagen, Denmark, September, 2007.
9. Fluent 12 User’s Guide, ANSYS Inc., 2010.
10. R.H. PERRY, D.W. GREEN, *Perry’s Chemical Engineers’ Handbook*, McGraw-Hill Professional, 2007.
11. D.S. DANDY, H.A. DWYER, *A sphere in shear flow at finite Reynolds number: effect of shear on particle lift, drag, and heat transfer*, Journal of Fluid Mechanics, **216**, 381–410, 1990.

12. H.K. MOFFATT, *Viscous and resistive eddies near a sharp corner*, Journal of Fluid Mechanics, **18**, 1–18, 1964.
13. A. MCD. MERCER, *Moffatt eddies in viscous flow through a curved tube of square cross-section*, AIChE Journal, **32**, 159–162, 2004.
14. W.R. DEAN, *Note on the motion of fluid in a curved pipe*, Phil. Mag., **20**, 208–223, 1927.
15. S. KIM, S.J. LEE, *Measurement of Dean flow in a curved micro-tube using micro digital holographic particle tracking velocimetry*, Exp. Fluids, **46**, 255–264, 2009.
16. K. YAMAMOTO, X. WU, K. NOZAKI, Y. HAYAMIZU, *Visualization of Taylor–Dean flow in a curved duct of square cross-section*, Fluid Dynamics Research, **38**, 1–18, 2006.
17. C.D. MEINHART, S.T. WERELEY, J.G. SANTIAGO, *Volume illumination for two-dimensional Particle Image Velocimetry*, Meas. Sci. Technol., **11**, 809–814, 2000.
18. J.B. KNIGHT, A. VISHWANATH, J.P. BRODY, R.H. AUSTIN, *Hydrodynamic Focusing on a Silicon Chip: Mixing Nanoliters in Microseconds*, Phys. Rev. Lett., **80**, 3863–3866, 1998.
19. A.E. KAMHOLZ, P. YAGER, *Theoretical Analysis of Molecular Diffusion in Pressure-Driven Laminar Flow in Microfluidic Channels*, Biophysical Journal, **80**, 155–160, 2001.
20. J.B. SALMON, A. AJDARI, *Transverse transport of solutes between co-flowing pressure-driven streams for microfluidic studies of diffusion/reaction processes*, Journal of Applied Physics, **101**, 074902, 2007.
21. R.F. ISMAGILOV, A.D. STROOCK, P.J.A. KENIS, G. WHITESIDES, *Experimental and theoretical scaling laws for transverse diffusive broadening in two-phase laminar flows in microchannels*, Appl. Phys. Lett., **76**, 2376–2378, 2000.

Received June 7, 2010; revised version December 20, 2010.
